



# Theoretical Modeling and Experimental Characterization of a 3D-Printed Solid Fuel grains for Ramjet applications

Sasi Kiran Palateerdham, Francesco Renzulli, Daniele Rapacciuolo, Daniele Tortorici, Antonella Ingenito<sup>5</sup>

#### **Abstract**

The solid-fuel ramjet (SFRJ) motor is a favorable air-breathing propulsion system and a promising option for extending the speed and range of military applications such as ramjet-powered missiles. Owing to its simple structure, the SFRJ provides a reliable means of propulsion; however, operation at high altitudes introduces challenges such as ignition difficulty and blowout due to low ambient pressure. To address these issues, a wide range of solid fuels has been investigated, focusing on improving flammability and enabling flexible manufacturing to meet structural requirements. Additive manufacturing (3D printing) offers significant advantages in this context by allowing precise control over grain geometry and internal fuel composition compared to conventional casting methods. In this work, polylactic acid (PLA) based solid fuels with different port geometries were fabricated using 3D printing and tested under an oxygen environment in a laboratory-scale hybrid rocket setup. The experimental campaign enabled the measurement of combustion chamber pressure, thrust, and fuel regression rate, providing insights into the performance characteristics of additively manufactured solid fuels and laying the groundwork for future application in SFRJ engines.

**Keywords:** Air-breathing propulsion, Solid fuel ramjet, test facility development, 3D printing, Fuel grain regression.

### 1. Introduction

Solid-fuel ramjet (SFRJ) propulsion systems combine structural simplicity, reliability, and cost-effectiveness, making them attractive for a variety of aerospace applications. Unlike conventional propulsion systems, SFRJs achieve high specific impulse without the need for complex fuel control, storage, or feed mechanisms. Their design leverages air-breathing, subsonic combustion with minimal moving parts, resulting in a low-cost and dependable system [1, 2]. A typical SFRJ consists of a cylindrical body filled with solid fuel and a diffuser that compresses incoming air, which then reacts with the grain surface to sustain combustion and generate thrust [3, 4].

Beyond their simplicity, SFRJs also offer high energy density, making them well-suited for supersonic propulsion. However, accurate design and performance prediction remain challenging, particularly under off-design conditions. These challenges stem from the strong coupling between fuel grain geometry, flame structure, and regression behavior—factors that critically govern overall engine performance[5].

Traditional grain shapes, while easier to model and manufacture, often fall short in terms of flameholding capabilities and robustness under varying operational regimes. More intricate geometries could improve flame stabilization and widen the operational envelope of these systems. However, such shapes are difficult to produce using conventional manufacturing methods. The emergence of additive manufacturing

<sup>&</sup>lt;sup>1</sup>Ph.D., Sapienza University of Rome, Italy, sasikiran.palateerdham@uniroma1.it

<sup>&</sup>lt;sup>2</sup>Engg., Space Frontier srl, Italy, francesco.renzulli@spacefrontier.eu

<sup>&</sup>lt;sup>3</sup>Engg., Space Frontier srl, Italy, daniele.rapacciuolo@spacefrontier.eu

<sup>&</sup>lt;sup>4</sup>Ph.D., Sapienza University of Rome, Italy, daniele.tortorici@uniroma1.it

<sup>&</sup>lt;sup>5</sup>Professor., Sapienza University of Rome, Italy, antonella.ingenito@uniroma1.it

provides a viable path to realize these complex geometries, potentially enabling better performance control [6].

According to the open literature, numerous studies have investigated various aspects of solid-fuel ramjet engines, including combustor geometry [7], fuel formulation [8], swirling flow effects [9], and inlet conditions [10], in order to better understand fuel regression rates and overall engine performance. Despite this, there is a noticeable lack of research specifically addressing the 3D printed different fuel port shapes for solid-fuel ramjet applications.

This study presents a novel approach that combines experimental characterization of a 3D-printable solid fuel with varying port geometries to investigate regression behavior in a solid-fuel ramjet combustor. A filament suitable for additive manufacturing was developed and characterized through lab-scale pyrolysis tests using thermal analysis techniques. The results capture key physical behaviors, including melting point and performance sensitivity, providing valuable insights into combustion physics. By leveraging additive manufacturing, this approach enables the exploration of complex, performance-optimized grain geometries that were previously impractical to produce. The findings establish a foundation for future research aimed at improving flame holding and extending the operability of solid-fuel ramjets under off-design conditions.

## 2. Theoretical modelling of solid fuels regression rates in hybrid engines

In this section, a physics-based mathematical model for the regression rate,  $\dot{r}$  (m s<sup>-1</sup>), has been developed. The theoretical approach accounts for the energy balance between conductive heat flux into the solid, convective heat transfer from the flame to the grain, and radiative exchange with the high-temperature reacting gases[11, 12, 13].

This governing energy-balance equation is formulated to yield a generic, explicit expression for the regression rate as a function of the propellant's thermophysical properties, initial conditions, and O/F combination. In particular, this equation accounts for the different heat transfer mechanisms, such as, pyrolysis of elastomeric fuels like HTPB; melting and liquid-film formation and entrainment effects for liquefying waxes, like for paraffin; and melting followed by thermal depolymerization/decomposition like for the thermoplastic PLA.

At the gas-solid interface the steady, local energy balance reads

$$q_{\mathsf{conv}}^{\prime\prime} + q_{\mathsf{rad}}^{\prime\prime} = \rho_s \, \dot{r} \, h_p + q_{\mathsf{cond,s}}^{\prime\prime},\tag{1}$$

where  $\rho_s$  is the solid density and  $h_p$  the effective heat of pyrolysis/vaporization (including latent and endothermic decomposition contributions)),  $T_p$  is the pyrolysis temperature. Conduction into the solid can be linearized as

$$q_{\text{cond s}}^{"} \approx \rho_s c_{p,s} \dot{r} (T_p - T_0),$$
 (2)

with  $c_{p,s}$  the solid specific heat and  $T_0$  the solid initial temperature. Hence

$$q''_{\text{conv}} + q''_{\text{rad}} = \rho_s \, \dot{r} \left[ h_p + c_{p,s} (T_p - T_0) \right].$$
 (3)

The convective heat flux is given by:

$$q_{\mathsf{conv}}^{\prime\prime} = \rho_q u \, c_{p,q} \left( T_f - T_p \right) \mathsf{St}. \tag{4}$$

where the Stanton-number correction accounts for the effect of the gaseous fuel ejection from the wall that introduces a normal mass flux resulting in a reduced oxidizer flow rate at the surface and weakens near-wall gradients, thereby reducing convective heat transfer [14, 15].

This blowing effect is characterized by the Spalding mass-transfer number:

$$B_m \equiv \frac{Y_{f,w} - Y_{f,\infty}}{1 - Y_{f,w}} \approx \frac{\dot{m}_f''}{G} = \frac{\rho_s \dot{r}}{G}, \tag{5}$$

where  $\dot{m}_f''=\rho_s\dot{r}$  is the fuel mass flux emitted per unit area and  $G=\rho_g u$  is the gas-phase mass flux.

As  $B_m$  increases, the effective convective transfer is reduced. In turbulent flow, this is modeled by:

St = 
$$\frac{\text{St}_0}{(1+B_m)^m}$$
,  $m \simeq 0.7-1.0$ , (6)

where, the no-blowing Stanton number St<sub>0</sub> may be calculated by

$$\operatorname{Nu}_x = 0.0296 \operatorname{Re}_x^{0.8} \operatorname{Pr}^{1/3}, \qquad h_x = \frac{\operatorname{Nu}_x k_g}{x}, \qquad \operatorname{St}_0 = \frac{h_x}{\rho_g u c_{p,g}},$$
 (7)

with  $\mathrm{Re}_x = \rho_g ux/\mu_g$  and x a local axial length (a hydraulic-diameter formulation can be used equivalently).

The contribution of the radiation from the flame to the wall has been modeled assuming the propellant as gray body:

$$q_{\mathsf{rad}}^{\prime\prime} = \varepsilon_{\mathsf{eff}} \, \sigma \left( T_f^4 - T_p^4 \right), \tag{8}$$

where  $\varepsilon_{\rm eff}$  is the gas or soot emissivity and  $\sigma$  is the Stefan–Boltzmann constant.

Combining the above equations gives:

$$\dot{r} = \frac{\rho_g u c_{p,g} (T_f - T_p) \frac{\mathsf{St}_0}{\left(1 + \frac{\rho_s \dot{r}}{G}\right)^m} + \varepsilon_{\mathsf{eff}} \sigma \left(T_f^4 - T_p^4\right)}{\rho_s \left[h_p + c_{p,s} (T_p - T_0)\right]},\tag{9}$$

which is solved mathematically at each axial station.

This equation may be used and is valid for different fuels.

As an example, for pyrolyzing elastomers such as HTPB, Eq. (9) is:

$$h_{\text{eff}} \approx h_p + c_{n,s}(T_p - T_0) \tag{10}$$

For liquefying fuels, instead, such as paraffin, additional heat for liquefying is required, and Eq. (9) becomes:

$$h_{\text{eff}} = c_{n.s}(T_m - T_0) + h_m + c_{n,\ell}(T_p - T_m) + h_p \tag{11}$$

Furthermore, in liquefying fuels, droplets are ejected into the stream, enhancing near-wall mixing and increasing the effective heat feedback beyond that predicted by convection (entrainment). A convenient closure augments the convective heat flux by a multiplicative factor,

$$q_{\text{conv.eff}}^{"} = \Phi_e \, q_{\text{conv}}^{"}, \qquad \Phi_e \ge 1,$$
 (12)

where  $q''_{\text{conv}} = \rho_g u \, c_{p,g} \, (T_f - T_m)$  St is the no-entrainment convective term. The amplification factor  $\Phi_e$  is an order-unity quantity that increases with wall shear and decreases with melt viscosity:

$$\frac{\partial \Phi_e}{\partial \tau_w} > 0, \qquad \frac{\partial \Phi_e}{\partial \mu_\ell} < 0,$$
 (13)

where  $\tau_w=\rho_g u_\tau^2=\frac{1}{2}\rho_g u^2 C_f$  is the wall shear stress (expressed via friction velocity  $u_\tau$  or friction coefficient  $C_f$ ) and  $\mu_\ell$  is the liquid-film viscosity.

Two practical parameterizations (to be calibrated against data) are:

(i) Power law in shear/viscosity: 
$$\Phi_e = 1 + C_e \left(\frac{\tau_w}{\tau_{\rm ref}}\right)^a \left(\frac{\mu_{\rm ref}}{\mu_\ell}\right)^b, \quad a,b>0,$$
 (14)

(ii) Film-Reynolds form: 
$$\Phi_e = 1 + \tilde{C}_e \operatorname{Re}_{\ell}^{\alpha}, \qquad \operatorname{Re}_{\ell} = \frac{\rho_{\ell} u_w \delta_{\ell}}{\mu_{\ell}},$$
 (15)

with  $C_e, \tilde{C}_e, a, b, \alpha$  determined by regression;  $u_w$  and  $\delta_\ell$  denote the interfacial (slip) velocity and the melt-film thickness.

Because  $\Phi_e$  is a modeling shortcut, it can be inferred a posteriori from measured regression rates using the local energy balance:

$$\rho_s \dot{r} h_{\text{eff}} = q''_{\text{conv.eff}} + q''_{\text{rad}} = \Phi_e q''_{\text{conv}} + q''_{\text{rad}}, \tag{16}$$

which yields

$$\Phi_e = \frac{\rho_s \, \dot{r} \, h_{\text{eff}} - q_{\text{rad}}^{"}}{q_{\text{conv}}^{"}} = \frac{\rho_s \, \dot{r} \, h_{\text{eff}} - \varepsilon_{\text{eff}} \sigma \left( T_f^4 - T_m^4 \right)}{\rho_g u \, c_{p,g} \left( T_f - T_m \right) \, \text{St}} \tag{17}$$

Typical values reported for paraffin in cylindrical ports are  $\Phi_e \sim 1.1$ –2 depending on G, wall shear, and melt viscosity; more viscous films (e.g., PLA) tend to give  $\Phi_e \approx 1$  (weak entrainment).

$$q_{\mathsf{conv}}^{\prime\prime} \to \Phi_e \, q_{\mathsf{conv}}^{\prime\prime}, \quad \Phi_e \ge 1,$$
 (18)

with  $\Phi_e$  increasing with wall shear and decreasing with melt viscosity.

Including also the entrainment, the regression rate law reads:

$$\dot{r} = \frac{\Phi_e G c_{p,g} (T_f - T_p) \operatorname{St} + \varepsilon_{\text{eff}} \sigma \left( T_f^4 - T_p^4 \right)}{\rho_s h_{\text{eff}}}$$
(19)

PLA is a thermoplastic; therefore, melting and subsequent decomposition occur. In baseline configurations, PLA generally exhibits low entrainment (viscous melt) and therefore behaves closer to HTPB in terms of mixing enhancement while still carrying the fusion/sensible load of a melting fuel.

Eq. (9) shows that the regression rate increases whenever the net heat feedback to the wall grows through convection and radiation, or the surface energy load per unit mass decreases. On the convective side, larger oxidizer mass flux G and flow arrangements that raise the Reynolds and Nusselt numbers (for example, shorter local axial scale x, lower gas viscosity  $\mu_g$ , or port/injector architectures that induce swirl or transverse injection) enhance the heat-transfer coefficient  $h_x$  and the no-blowing Stanton number St\_0. The blowing correction St =  $\operatorname{St}_0/(1+B_m)^m$  attenuates the convective term; its penalty is mitigated as  $B_m = \rho_s \dot{r}/G$  decreases, which typically occurs at higher G for a given  $\dot{r}$ . A larger thermal driving, quantified by the difference  $T_f - T_p$ , directly amplifies  $q''_{\operatorname{conv}} = \Phi_e \, G \, c_{p,g} (T_f - T_p)$  St; this can be obtained via oxidizer and mixture-ratio choices that increase  $T_f$  or via material/chemical strategies that reduce the surface (pyrolysis) temperature  $T_p$ . Radiative feedback grows with the effective emissivity  $\varepsilon_{\mathrm{eff}}$  and with the radiative temperature  $T_r$ , reflecting the role of emitting species (H2O and CO2, and soot when present) through  $q''_{\mathrm{rad}} = \varepsilon_{\mathrm{eff}} \sigma (T_r^4 - T_p^4)$ . For liquefying fuels, entrainment augments near-wall mixing beyond pure convection; the effective gain is captured by  $\Phi_e > 1$ , which increases with wall shear and decreases with melt viscosity, thereby raising  $\dot{r}$  under high-shear, low-viscosity conditions.

The denominator  $\rho_s h_{\rm eff}$  embodies the energy required to sustain surface regression. Reducing  $h_{\rm eff}$  for example by lowering the pyrolysis/vaporization load  $h_p$  or by limiting sensible and latent terms associated with melting favors higher rates; conversely, larger  $h_{\rm eff}$  or higher solid density  $\rho_s$  depress  $\dot{r}$ . In practical terms, weaker convection (lower G, higher  $\mu_g$ , longer x) and stronger blowing (larger  $B_m$ ) reduce St, while smaller thermal driving (lower  $T_f$  or higher  $T_p$ ) and weaker radiation (smaller  $\varepsilon_{\rm eff}$ , lower  $T_r$ ) diminish the heat feedback. For liquefying fuels, a viscous melt suppresses droplet ejection, effectively driving  $\Phi_e \to 1$  and removing the entrainment benefit.

The most critical and sensitive parameters suggested by the model are the convective/flame temperature  $T_f$  and the surface temperature  $T_p$ , which together set both the convective driving and, indirectly, the surface energy budget; variations on the order of 100–200 K translate into changes in  $\dot{r}$ . Local convection (through Nu and  $h_x$ ) scales strongly with  $Re \propto G/\mu_g$ , making injector and port architecture a primary design lever. The blowing parameter  $B_m$  matters especially at low G and is consistent with

empirical exponents  $n\approx 0.6$ –0.7 observed in  $\dot{r}=a\,G^n$ . For liquefying fuels, the entrainment factor  $\Phi_e$  is governed by melt viscosity  $\mu_\ell$  and wall shear  $\tau_w$ , both addressable via formulation and flow design. Finally, the choice of oxidizer and O/F sets  $T_f$ , gas properties  $(c_{p,g},k_g,\mu_g)$ , and emissivity, thereby coupling thermochemistry and transport to the observed regression.

These considerations point to several promising directions for development: optimization of flow architecture (swirl, multi-port, transverse injection, and tailored axial scales) to maximize Nu where beneficial; consistent thermochemical evaluation of  $T_f$  and gas properties as functions of O/F for each oxidizer, including finite-rate and finite-Schmidt effects when necessary; engineering of melt-film rheology in liquefying fuels (blends, additives, fillers, surface texturing) to tune  $\Phi_e$ ; targeted manipulation of material energetics (controlling  $h_p$ , sensible/fusion contributions, and  $T_p$ ) to adjust  $h_{\rm eff}$ ; and radiative management via emissive or low-emissivity strategies. A systematic uncertainty and sensitivity quantification on  $T_f$ ,  $T_p$ ,  $\mu_g$ , and  $\varepsilon_{\rm eff}$  is recommended to ensure robustness of design predictions based on the model.

In order to define and validate the regression-rate equation, Table 1 reports a selection of representative solid-fuel properties.

Table 1. Solid-fuel properties

Material	$ ho_s$ [kg m $^{-3}$ ]	$c_{p,s}$ [J kg $^{-1}$ K $^{-1}$ ]	$T_m$ [K]	$h_{m}$ [kJ kg $^{-1}$ ]
PLA	1240	1800	433	110-140

In order to provide a quick comparison of oxidizer-to-fuel ratios (O/F), a  $CH_2$  surrogate is considered for the fuel. In fact, these polymeric/hydrocarbon fuels, for first-order stoichiometric estimates, may be assumed as a repeating  $-CH_2$ — units. With the  $CH_2$  surrogate, the stoichiometric reactions are:

 $\mathbf{O}_2$ :

$$\mathrm{CH_2} + \tfrac{3}{2}\,\mathrm{O_2} \ \longrightarrow \ \mathrm{CO_2} + \mathrm{H_2O}, \qquad \mathrm{O/F_{stoich}} = \frac{1.5\,M_{\mathrm{O_2}}}{M_{\mathrm{CH_2}}} \approx 3.42.$$

 $N_2O$ :

$${\rm CH_2} + 3\,{\rm N_2O} \ \longrightarrow \ {\rm CO_2} + {\rm H_2O} + \tfrac{3}{2}\,{\rm N_2}, \qquad {\rm O/F_{\rm stoich}} = \frac{3\,M_{\rm N_2O}}{M_{\rm CH_2}} \approx 9.41.$$

H<sub>2</sub>O<sub>2</sub> (100%):

$${\rm CH_2} + 3\,{\rm H_2O_2} \ \longrightarrow \ {\rm CO_2} + 2\,{\rm H_2O}, \qquad {\rm O/F_{\rm stoich}} = \frac{3\,M_{\rm H_2O_2}}{M_{\rm CH_2}} \approx 7.27.$$

Air (taken as 23.2%  $O_2$  by mass):

$${
m O/F_{stoich}(air)} = rac{1.5\,M_{
m O_2}}{0.232\,M_{
m CH_2}} \, pprox \, 14.75.$$

These  $CH_2$ -based relations provide just a baseline to compare O/F across fuels and oxidizers. Table 2 gives stoichiometric mass O/F for a  $CH_2$  surrogate with common oxidizers, useful for scoping mixture ratios; air is taken at 23.2%  $O_2$  by mass.

**Table 2.** Stoichiometric oxidizer-to-fuel ratio (O/F, mass) for  $CH_2$  with various oxidizers.

Oxidizer	O/F <sub>stoich</sub>	
$O_2$	3.42	
$N_2O$	9.41	
$H_2O_2$ (100%)	7.27	
Air	14.75	

To extract reference coefficients in the form  $\dot{r} = a \, G^n$  from Eq. (9), three different fuels (Table 3) at the input data reported in (Table 4) are considered.

**Table 3.** Solid-fuel thermophysical properties

Parameter	PLA
Solid density, $ ho_s$ [kg m $^{-3}$ ]	1240
Solid $c_p$ , $c_{p,s}$ [J kg $^{-1}$ K $^{-1}$ ]	1800
Liquid $c_p$ , $c_{p,\ell}$ [J kg $^{-1}$ K $^{-1}$ ]	2000
Melting point, $T_m$ [K]	433
Latent heat of fusion, $h_{m}$ [kJ kg $^{-1}$ ]	120
Pyrolysis temperature, $T_p$ [K]	
Grain temperature, $T_0$ [K]	300
Effective pyrolysis load, $h_p$ [kJ kg $^{-1}$ ]	250
Entrainment factor, $\Phi_e$ [–]	1.0
Effective emissivity, $\varepsilon_{\rm eff}$ [-]	0.10

**Table 4.** Flow inputs (common to all fuels)

Quantity	Symbol (units)	Value
Mass-flux range	$G$ [kg m $^{-2}$ s $^{-1}$ ]	50–300
Gas dynamic viscosity	$\mu_g$ [Pas]	$4.0 \times 10^{-5}$
Gas thermal conductivity	$k_g$ [W m $^{-1}$ K $^{-1}$ ]	0.10
Prandtl number	Pr [–]	0.70
Gas specific heat	$c_{p,g}$ [J $\mathrm{kg}^{-1}\mathrm{K}^{-1}$ ]	1200
Local axial length (or scale)	x [m]	0.10
Flame temperature	$T_f$ [K]	2500
Blowing exponent (turbulent)	m [-]	0.8
Unit conventions	$G_{\mathrm{[g/cm^2/s]}} = 0.1G_{\mathrm{[kg/m^2/s]}}$ ,	
		$\dot{r}_{[\mathrm{mm/s}]} = 10^3  \dot{r}_{[\mathrm{m/s}]}$

Assuming  $G=200 \text{ kg m}^{-2} \text{ s}^{-1}$ , for the values given in the previous tables:

$$\mathrm{Re}_x = \frac{Gx}{\mu_g} = \frac{200 \cdot 0.10}{4 \times 10^{-5}} = 5.0 \times 10^5, \qquad \mathrm{Nu}_x = 0.0296 \, \mathrm{Re}_x^{0.8} \mathrm{Pr}^{1/3} \approx 953,$$

$$h_x = \frac{\mathsf{Nu}_x k_g}{x} \approx 953 \; \mathsf{W} \, \mathsf{m}^{-2} \mathsf{K}^{-1}, \qquad \mathsf{St}_0 = \frac{h_x}{G c_{p,g}} \approx \frac{953}{200 \cdot 1200} = 3.97 \times 10^{-3}.$$

By substituting the values from Tables 3 and 4 into 19, the results reported below are obtained.

**Table 5.** Theoretical results for  $(\dot{r} \text{ in mm s}^{-1})$ 

Fuel	$a~\mathrm{[mms^{-1}]}$	n [-]
PLA (conservative)	0.182	0.673

**Table 6.** a, n units:  $\dot{r}$  in mm s<sup>-1</sup>, G in g cm<sup>-2</sup> s<sup>-1</sup>.

Fuel	This model		Example literature	
	a	n	a	n
PLA (conservative)	0.182	0.673	lower i	rates; limited data

From these a, n theoretical values, the regression rate as a function of GOx is obtained (see Table ??).

**Table 7.** Regression rate  $\dot{r}$  (mm s<sup>-1</sup>) versus oxidizer mass flux G (kg m<sup>-2</sup> s<sup>-1</sup>) for PLA, with  $T_f = T_r = 1800$  K.

$G\left[ kgm^{-2}s^{-1} \right]$	PLA $\dot{r}$ [mm s $^{-1}$ ]	
50	0.283	
75	0.377	
100	0.463	
125	0.546	
150	0.626	
175	0.702	
200	0.777	
225	0.850	
250	0.921	
275	0.991	
300	1.060	

Using the same gas-side and material inputs of Tables 4–3, the implicit balance in Eq. (9) was re-solved, setting the convective and radiative temperatures to  $T_f=T_r=1800$  K. The resulting regression-rate curves  $\dot{r}(G)$  were then fitted to the empirical law  $\dot{r}=a\,G^n$  with  $\dot{r}$  in mm s<sup>-1</sup> and G in g cm<sup>-2</sup> s<sup>-1</sup>.

**Table 8.** Back-calculated power-law coefficients at  $T_f = T_r = 1800$  K ( $\dot{r} = a \, G^n$ , with  $\dot{r}$  in mm s<sup>-1</sup> and G in g cm<sup>-2</sup> s<sup>-1</sup>).

Fuel	$a \ [mm  s^{-1}  (g  cm^{-2}  s^{-1})^{-n}]$	n [-]
PLA	0.085	0.739

As a consistency check at  $G=200~{\rm kg\,m^{-2}\,s^{-1}}$  ( $G=20~{\rm g\,cm^{-2}\,s^{-1}}$ ), the fitted curves give  $\dot{r}_{\rm HTPB}\approx 1.07~{\rm mm\,s^{-1}}$ ,  $\dot{r}_{\rm PLA}\approx 0.78~{\rm mm\,s^{-1}}$ ,  $\dot{r}_{\rm Paraffin}\approx 2.05~{\rm mm\,s^{-1}}$ , in close agreement with the direct solution of Eq. (9) (see Table 9).

**Table 9.** Regression rate  $\dot{r}$  (mm s<sup>-1</sup>) versus oxidizer mass flux G (kg m<sup>-2</sup> s<sup>-1</sup>) for PLA, with  $T_f = T_r = 1800$  K.

$G\left[ kgm^{-2}s^{-1} \right]$	PLA $\dot{r}$ [mm s $^{-1}$ ]
50	0.283
75	0.377
100	0.463
125	0.546
150	0.626
175	0.702
200	0.777
225	0.850
250	0.921
275	0.991
300	1.060

At  $T_f=T_r=1800$  K the HTPB fit lies close to representative oxygen-based datasets (e.g.  $\dot{r}\approx 1.12$  mm s $^{-1}$  at G=20 g cm $^{-2}$  s $^{-1}$  for a=0.146, n=0.681), reflecting the strong sensitivity of  $\dot{r}$  to the convective/radiative temperature levels embedded in the model.

## 3. Grain preparation method

The 3D printing process for grain manufacturing can be categorized into monomaterial and multimaterial approaches.

In the monomaterial process, a CAD model of the grain is first created according to the desired dimensions and then imported into slicer software, which generates the G-code required for printing. The slicer allows control over printing parameters such as density and layer height. Special attention must be given to the material profile, including the bed temperature and extrusion temperature, to ensure proper printing.

For the multimaterial process, the constraints of the combustion chamber are first input into MATLAB scripts, which generate the grain geometry accordingly [ refer to figure 1]. By default, the MATLAB scripts create twisted star ports, allowing the user to define the number of points and their dimensions. Separate STL files are created for each material. These files are then loaded into the Prusa Slicer in multimaterial mode, where each material's properties are defined. Finally, the slicer generates the G-code, which is loaded into the printer for fabrication.

## 4. Thermal analysis

Thermal analysis was employed in this study on polylactic acid (PLA) to evaluate the combustion-relevant properties of the fuel samples. The PLA samples were extracted from 3D printed grains both before and after combustion. Each test was carried out in triplicate to ensure reproducibility and enable statistical analysis.

The analysis included Thermogravimetric Analysis (TGA) and Differential Scanning Calorimetry (DSC), performed using a TGA/DSC 3+ analyzer (METTLER TOLEDO, Greifensee, Switzerland). The tests were conducted under a controlled nitrogen atmosphere with a flow rate of 50 mL/min. Approximately 10-15

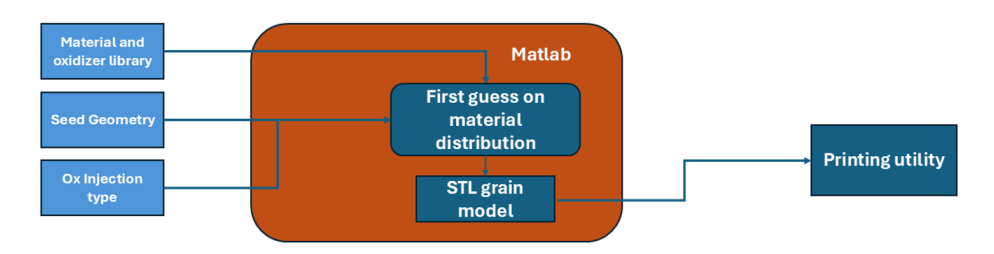
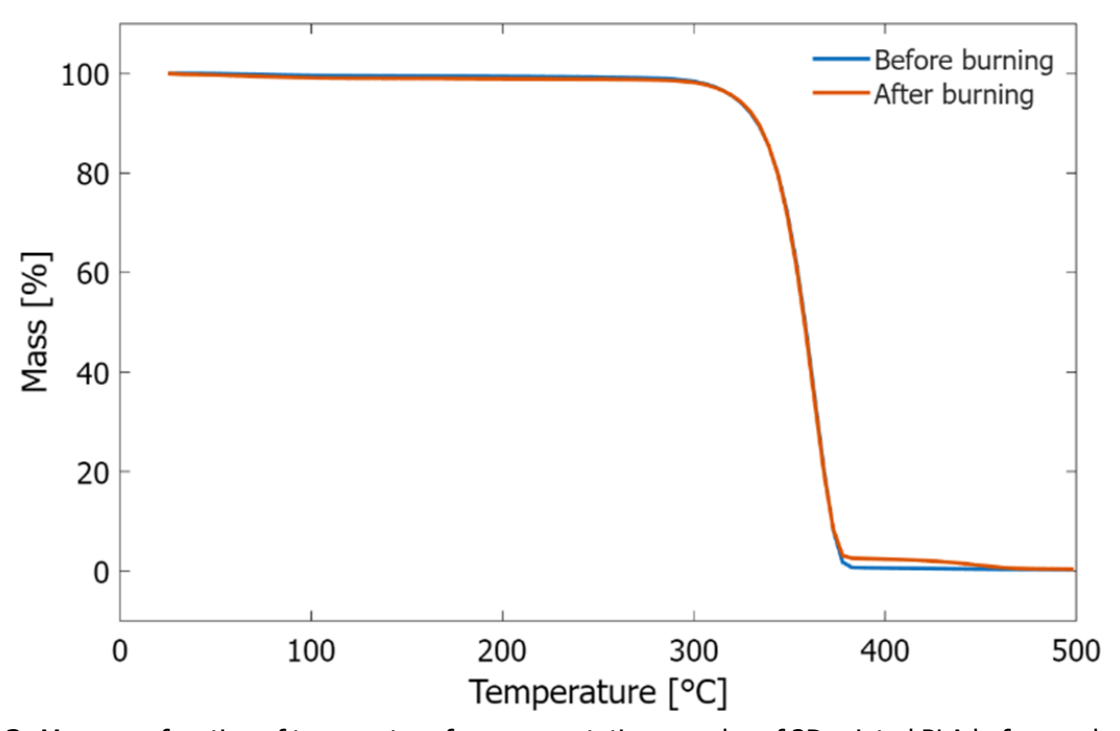


Fig 1. Automated Geometry Generation via MATLAB Scripting

milligrams of each sample was heated from room temperature to  $500\,^{\circ}\text{C}$  at a constant heating rate of  $10\,^{\circ}\text{C}/min$ . Mass loss and heat flow as a function of temperature were recorded to evaluate the thermal decomposition behavior.

Thermographs were analyzed to identify characteristic decomposition stages and onset temperatures. The melting temperature was determined from the first endothermic peak, while the vaporization temperature corresponded to the second endothermic peak.

As shown in Figure 2, TGA revealed similar thermal decomposition behavior for PLA before and after burning. The onset decomposition temperatures were  $346.1\pm3.4\,^{\circ}\text{C}$  before burning, and  $343.0\pm0.8\,^{\circ}\text{C}$  after burning.



**Fig 2.** Mass as a function of temperature for representative samples of 3D printed PLA before and after burning

A small residue ( $\sim 2\%$ ) persisted at higher temperatures after combustion, indicating the presence of residual compounds. This residue disappears at higher temperatures (above  $450\,^{\circ}\text{C}$ ).

The DSC analysis, shown in Figure 3, revealed a slight variation in the melting temperature of the material before and after combustion. Specifically, the melting temperature of PLA before combustion was  $147.8 \pm 5.2$  °C, increasing to  $155.8 \pm 0.9$  °C after combustion, suggesting possible changes in the

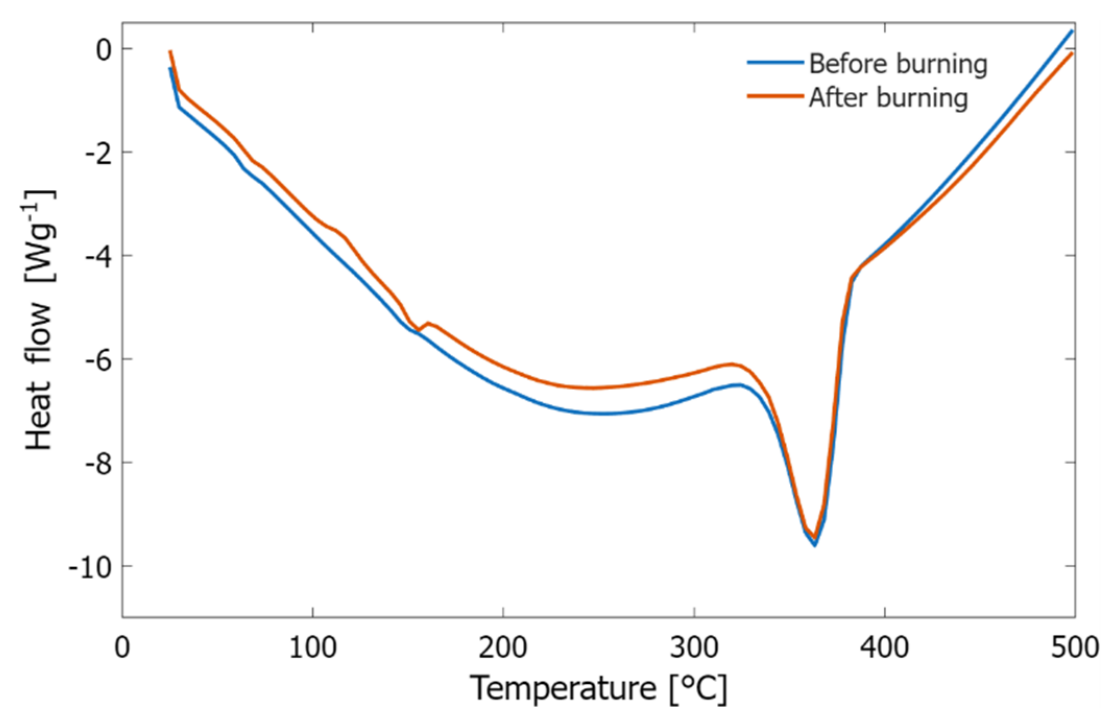


**Fig 3.** Heat flow as a function of temperature for representative samples of 3D printed PLA before and after burning

polymer structure or the retention of combustion by-products that may influence the thermal transition. In contrast, the vaporization temperature remained nearly unchanged, with values of  $370.7 \pm 1.9\,^{\circ}\text{C}$  before and  $370.0 \pm 0.4\,^{\circ}\text{C}$  after combustion, indicating that the thermal behavior at higher temperatures was not significantly affected by the burning process.

## 5. Development plan for the Experimental Setup

A direct connected test facility has been designed and is under construction, as shown in fig4. In this setup, the ramjet engine is connected directly to an air supply system that can simulate the high speed airflow conditions typical of ramjet operation. This configuration allows for experiments to be conducted at various simulated flight speeds and altitudes without the need for actual flight tests. By replicating the high dynamic pressures and temperatures experienced during flight, this facility provides invaluable data on the ramjet engine's performance under real-world conditions [16].

The schematic of the test facility, shown in the figure below, illustrates the comprehensive setup used for these experiments.

This consists of the following main components:

- 1. **Air Supply System:** The facility includes a high-capacity air compressor and 10  $m^3$  storage tanks to provide a continuous and regulated airflow. This air supply system can adjust the pressure and flow rate to different flight conditions.
- 2. **Heaters and Conditioners:** Before reaching the ramjet, the air passes through an air vitiator to achieve the desired temperature, simulating the thermal conditions encountered at high speeds and altitudes.
- 3. **Combustor:** The ramjet's combustor is designed to operate under controlled conditions. Solid Fuel is positioned within the combustor. Hot air at the required pressure enters the combustion chamber, reacts with the grain, and the exhaust is expanded through the nozzle to produce enough

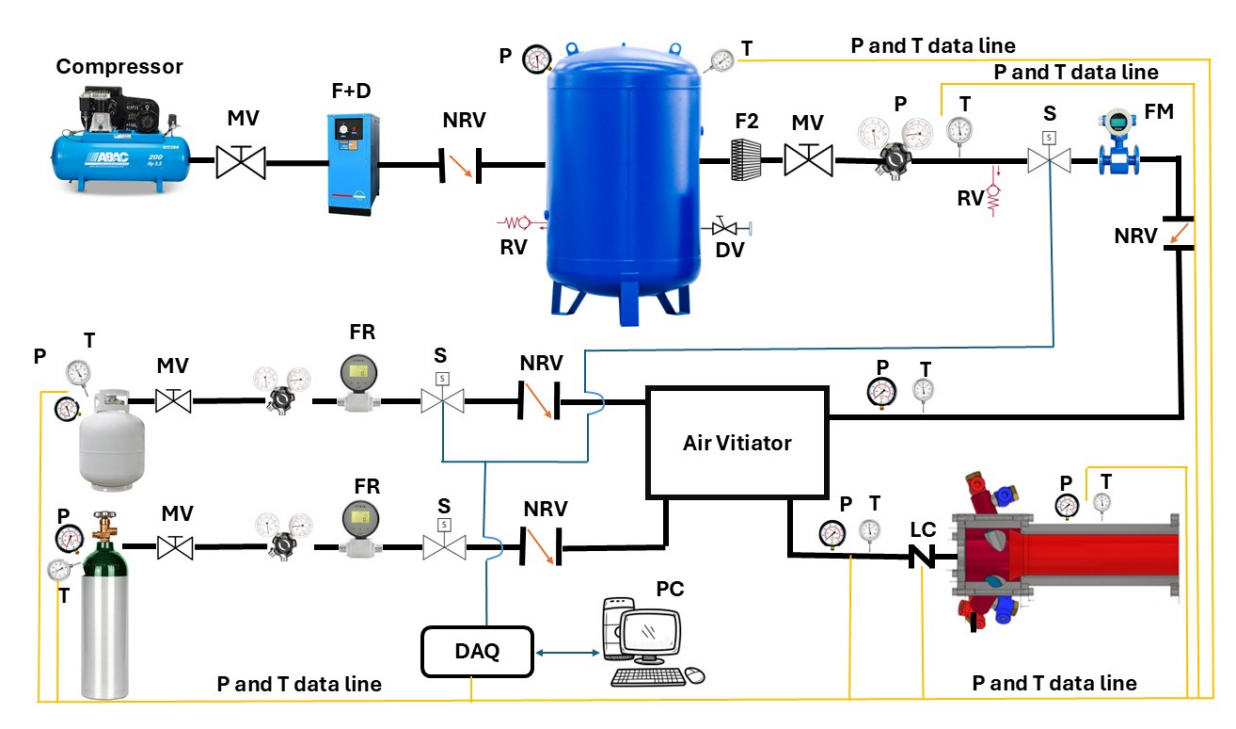


Fig 4. Schematic of the Direct-Connected Test Facility

thrust

4. **Instrumentation and Data Acquisition:** The facility is outfitted with advanced instrumentation, including pressure transducers, load cells, thermocouples, a high-speed camera, an exhaust analyser, and flow meters, to capture real-time data. A data acquisition system collects and records this information for analysis

# 6. Ballastic fire testing

To further assess the performance of these 3D-printed solid fuel grains, a series of ballistic tests was performed using gaseous oxygen as the oxidizer in a laboratory-scale static hybrid rocket motor. The experimental setup consisted of a lab-scale motor mounted on a thrust stand, an oxidizer supply system, a pyrogen igniter, and a data acquisition system. A schematic of the configuration is presented in 5. The oxidizer was delivered into the combustion chamber via a stainless-steel axial flow injector. Ignition was achieved using the pyrogen igniter located at the head end of the motor, producing sufficient heat to surpass the fuel grain's ignition temperature. This process preheats the chamber, allowing the fuel to vaporize and react efficiently with the incoming oxidizer.

The combustion chamber was designed with an inner diameter of 80 mm and a length of 240 mm to house the solid fuel grain. A convergent–divergent nozzle was incorporated, with a 12 mm throat diameter, a semi-convergent angle of  $45^{\circ}$ , and a semi-divergent angle of  $13^{\circ}$ . Oxidizer delivery was controlled by a pressure regulator coupled with a solenoid valve. Each ballistic test was conducted with a burn duration of 5 s. After firing, the remaining fuel grain was easily extracted from the chamber using cardboard tubes, enabling precise post-test analysis. This allowed accurate determination of both the fuel regression rate and the total mass consumed.

The weight loss technique is one of the most reliable and convenient methods for measuring the regression rate in hybrid rocket engines. It has been widely adopted by researchers for this purpose [17]. This approach involves determining the regression rate by measuring the initial and final masses of the solid fuel grain. In the present study, the weight loss method is used to calculate the fuel regression

rate. After conducting the ballistic test, the engine is allowed to cool for at least 30 minutes. The nozzle is then dismantled, and the solid fuel grain is carefully removed. The final mass of the fuel is measured, and the difference between the initial mass (before the burn) and the final mass (after the burn) provides the total mass loss during the fire test. Dividing this net mass loss by the burn time yields the fuel mass consumption rate. The regression rate of the engine is subsequently determined as described in Eq.(20).

$$\dot{r} = \frac{d_b - d_{ig}}{2t_h} \tag{20}$$

Where  $d_b$  and  $d_{ig}$  are the fuel port diameters after burnout and before the ignition process, respectively. The burn time  $t_b$  is the time duration of the combustion, i.e., the start of ignition to the end of the oxidiser supply. The fuel port diameter after burnout can be given as in Eq.(21).

$$d_b = \sqrt{d_{ig}^2 + \frac{m_b}{\frac{\pi}{4}\rho_f l_f}} \tag{21}$$

Where  $m_b$  is the mass of burnt fuel and  $\rho_f$  is the actual measured density of the fuel, and  $l_f$  is the length of the fuel grain. The corresponding oxidiser mass flux rate can be given by Eq.(22).

$$G_{ox} = \frac{\dot{m}_{ox}}{A_n} \tag{22}$$

Where  $\dot{m}_{ox}$  is the oxidiser mass flow rate and  $A_p$  is the port combustion cross-section area, which can be calculated as given in Eq.(23).

$$A_p = \frac{\pi}{4} \left( \frac{d_b + d_{ig}}{2} \right)^2 \tag{23}$$

The combustion characteristics of 3D-printed solid propellant grains with cylindrical, helical, star, and multimaterial star port geometries were evaluated through static tests. Figure 6 presents the chamber pressure and thrust profiles for each port type, while Table 10 summarizes the ballistic parameters.

The tests consistently demonstrated three distinct phases:

- (i) a **ramp-up** phase driven by ignitor-assisted initial combustion, leading to a rise in chamber pressure;
- (ii) a **steady-state** phase, during which fuel combustion sustained pressure through heat release and gas generation; and
- (iii) a **cut-off** phase, marked by the cessation of oxygen supply and a rapid decrease in pressure and thrust.

Figure 6 (a) demonstrates that the cylindrical port grain exhibited a rapid ramp-up in chamber pressure reaching a steady-state value of approximately 2.5 Bar, with a corresponding thrust of 3000 g. The ramp-up phase was followed by a relatively stable steady-state region until cutoff. This behavior is consistent with the moderate regression rate of 0.2 mm/s and a port area of 0.000753  $m^2$ , resulting in an oxidizer mass flux of 18.78 kg/( $m^2 \cdot s$ ). The end-face of the grain after the test shows uniform regression along the circular port.

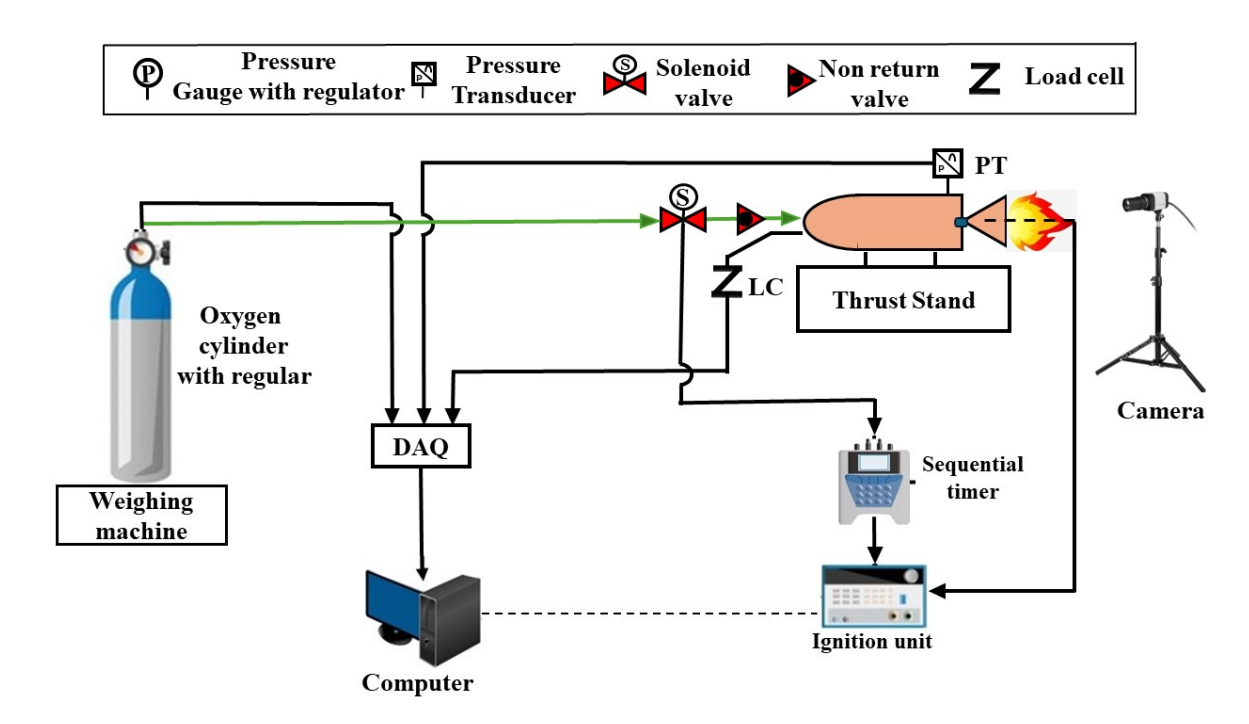


Fig 5. Schematic of hybrid rocket test facility at SIA ASPL

Figure 6 (b) The helical port configuration maintained a slightly increased chamber pressure ( $\sim$ 3 Bar) but with a smoother pressure trace and slightly lower thrust (2500–3000 g) compared to the cylindrical port. Its larger final diameter (0.0369 m) and port area (0.000880  $m^2$ ) lead to a higher oxidizer mass flux (20.46 kg/( $m^2 \cdot s$ )) and an improved regression rate (0.3 mm/s), indicating a slower but more controlled burn. The post-test grain image shows the helical groove structure largely intact, demonstrating minimal surface erosion along the helical path.

While Figure 6 (c) shows that the star-shaped port grain produced a higher chamber pressure ( $\sim$ 4 Bar) and sustained thrust around 3000 g. With a port diameter of 0.0368 m and a port area of 0.000876  $m^2$ , the star geometry achieved the highest oxidizer mass flux among single-material ports (31.96 kg/( $m^2 \cdot s$ )), while maintaining a similar regression rate (0.3 mm/s). The burn pattern produced the characteristic star-shaped cavity, indicating preferential regression along the port tips.

Figure 6 (d) shows the multimaterial star port showing the most energetic performance, with chamber pressures approaching 5 Bar and peak thrusts up to 4500 g. Its larger diameter (0.0398 m) and port area (0.000957  $m^2$ ) facilitated a higher oxidizer flux (25.08 kg/( $m^2 \cdot s$ )) than that of the first case and an increased regression rate of 0.5 mm/s. The end-face of the grain after testing reveals a well-defined star shape with heterogeneous regression, demonstrating the influence of multimaterial layering on burn dynamics.

These results highlight the influence of port geometry and material composition on combustion behavior. While cylindrical and helical ports provide stable and predictable performance, star-shaped geometries, particularly multimaterial designs, enable higher thrust and chamber pressures due to localized enhancement of the regression rate along the port tips.

#### 7. Conclusions

This study demonstrates that 3D-printed PLA grains with varied port geometries significantly influence Solid Fuel Ramjet performance. Thermal analysis of PLA grains before and after combustion shows that the material retains largely consistent decomposition behavior. TGA results indicate similar onset

**Table 10.** Port Types and Corresponding Ballistic Test Parameters

Port Type	Final diameter	Regression rate	Port area	Oxidizer mass flux
	$d_b$ [m]	$\dot{r}$ [mm/s]	$A_p$ [ $m^2$ ]	$G_{ox}$ [kg/(m $^2$ s)]
Cylindrical	0.0316	0.2	0.000753	18.7891
Helical	0.0369	0.3	0.000880	20.4639
Star	0.0368	0.3	0.000876	31.9605
Multimaterial Star	0.0398	0.5	0.000957	25.0824

decomposition temperatures (346.1  $\pm$  3.4 °C pre-combustion vs. 343.0  $\pm$  0.8 °C post-combustion) with only minor residue ( $\sim$ 2%), while DSC analysis shows a slight increase in melting temperature (147.8  $\pm$  5.2 °C to 155.8  $\pm$  0.9 °C) and an unchanged vaporization temperature ( $\sim$ 370 °C), suggesting minimal structural changes. Ballistic tests reveal that multi-material grains achieve regression rates 1.6–2.5 times higher than mono-material grains while maintaining internal geometry, highlighting enhanced combustion efficiency and structural integrity. Port geometry also plays a critical role: cylindrical and helical ports provide stable, uniform performance, whereas star-shaped ports—especially in multi-material designs—produce higher chamber pressures and peak thrust due to localized regression enhancements. These results demonstrate that multi-material 3D printing offers a scalable platform for precise control of combustion dynamics, improved thrust, and next-generation hybrid rocket and solid fuel ramjet applications.

#### **Acknowledgements**

The authors would like to acknowledge the SIA Advanced Space Propulsion Laboratory at the School of Aerospace Engineering - Sapienza University of Rome, in collaboration with Space Frontier S.r.l., Naples, Italy, for this joint collaborative work.

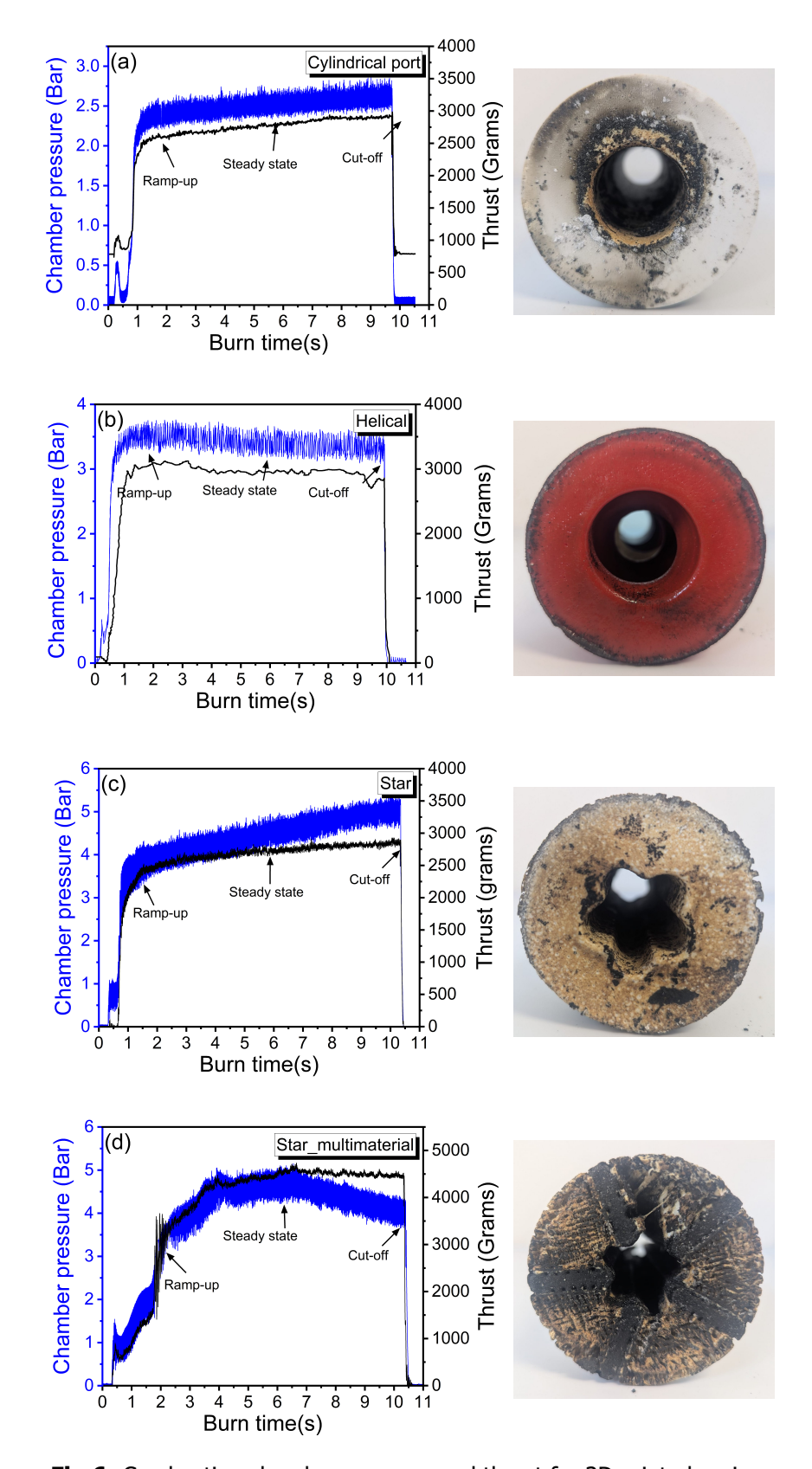


Fig 6. Combustion chamber pressure and thrust for 3D printed grains

#### References

- [1] Antonella Ingenito. Subsonic combustion ramjet design. Springer, 2021.
- [2] Sasi Kiran Palateerdham, Abdul Rahman, Antonella Ingenito, Sri Nithya Mahottamananda, and Yash Pal. Theoretical understanding of the effects of high-density energetic particles on the ramjet performance. Journal of Propulsion and Energy, 4(1):30–41, 2024.
- [3] H. Kadosh and B. Natan. Internal ballistics of a boron-containing solid fuel ramjet. Combustion Science and Technology, 193(15):2672–2691, 2020.
- [4] V. A. Azevedo, I. Alves, O. Shynkarenko, and C. A. G. Veras. Experimental investigation of high regression rate paraffin for solid fuel ramjet propulsion. In AIAA Propulsion and Energy 2019 Forum, 2019.
- [5] R. S. Fry. A century of ramjet propulsion technology evolution. Journal of Propulsion and Power, 20(1):27–58, 2004.
- [6] J. Patten, N. Padilla, C. R. Clark, P. Pecic, H. Bassett, D. Cruz, and K. A. Ahmed. Additively manufactured energetic solid fuels in airbreathing propulsion. In AIAA SCITECH 2025 Forum, 2025.
- [7] W. Li, X. Chen, O. Musa, L. Gong, and L. Zhu. Investigation of the effect of geometry of combustor on combustion characteristics of solid-fuel ramjet with swirl flow. Applied Thermal Engineering, 145:229–244, 2018.
- [8] B. McDonald, J. Rice, B. Hayes, C. Marshall, L. Pledger, D. Myers, and D. Jones. High density solid fuel ramjet fuel based on 1,6-hexanediol diglycidyl ether and methyltetrahydrophthalic anhydride. Fuel, 278:118354, 2020.
- [9] W. Li, X. Chen, D. Zhao, B. Wang, K. Ma, and T. Cai. Swirling effect on thermodynamic performance in a solid fueled ramjet with paraffin-polyethylene. Aerospace Science and Technology, 107:106341, 2020.
- [10] O. Musa, C. Xiong, Z. Changsheng, and W. Li. Effect of inlet conditions on swirling turbulent reacting flows in a solid fuel ramjet engine. Applied Thermal Engineering, 113:186–207, 2016.
- [11] G.A. Marxman and M. Gilbert. Turbulent boundary layer combustion in the hybrid rocket. In 9th International Symposium on Combustion, pages 371–383, New York, 1963. Academic Press.
- [12] M.A. Karabeyoglu, D. Altman, and B.J. Cantwell. Combustion of liquefying hybrid propellants: Part 1, general theory. Journal of Propulsion and Power, 18(3), 2002.
- [13] M.A. Karabeyoglu and B.J. Cantwell. Combustion of liquefying hybrid propellants: Part 2, stability of liquid films. Journal of Propulsion and Power, 18(3), 2002.
- [14] P. Estey, D. Altman, and J. McFarlane. An evaluation of scaling effects for hybrid rocket motors. In Proceedings of the 27th AIAA/ASME/SAE/ASEE Joint Propulsion Conference, Sacramento, CA, June 24–26 1991. AIAA Paper No. 91–2517.
- [15] L.D. Strand, M.D. Jones, R.L. Ray, and N.S. Cohen. Characterization of hybrid rocket internal heat flux and htpb fuel pyrolysis. In Proceedings of the 30th AIAA/ASME/SAE/ASEE Joint Propulsion Conference, Indianapolis, IN, June 27–29 1994. AIAA Paper No. 1994–2876.
- [16] Daniil Kalaev, Sasi Kiran Palateerdham, and Antonella Ingenito. Gas generator fuels for solid ramjet: Additive effects and their performance. In 11th European Conference for Aeronautics and Aerospace Sciences (EUCASS), Rome, Italy, 2025. Presented, proceedings not yet published.
- [17] Claudio Carmicino and Andrea R. Sorge. Role of injection in hybrid rockets regression rate behaviour. Journal of Propulsion and Power, 21(4):606–612, 2005.